Remote Forcing for a Circulation Pattern Favorable to Surface Melt over the Ross Ice Shelf

YINGFEI FANG,[a] SONG YANG,[a,b] XIAOMING HU,[a,b] SHUHENG LIN,[a] JAMES A. SCREEN,[c] AND SHANGFENG CHEN[d]

[a] *School of Atmospheric Sciences, Sun Yat-sen University, and Southern Marine Science and Engineering Guangdong Laboratory (Zhuhai), Zhuhai, Guangdong, China*
[b] *Guangdong Province Key Laboratory for Climate Change and Natural Disaster Studies, Zhuhai, Guangdong, China*
[c] *Department of Mathematics and Statistics, University of Exeter, Exeter, Devon, United Kingdom*
[d] *Center for Monsoon System Research, Institute of Atmospheric Physics, Chinese Academy of Sciences, Beijing, China*

(Manuscript received 3 March 2023, in final form 6 April 2024, accepted 28 May 2024)

ABSTRACT: The Ross Ice Shelf (RIS) experiences surface melt events in summer, which could accelerate ice loss and destabilize the ice sheet in a warming world. This study links the interannual variability of RIS surface melt to the northerly wind anomaly over the Ross Sea sector, which is established in association with the quasigeostrophic barotropic Rossby wave trains from the tropical Pacific and subtropical Australia toward West Antarctica. Atmospheric general circulation model experiments suggest that these Rossby wave trains are regulated by El Niño–related sea surface temperature (SST) anomalies in the tropical central–eastern Pacific and atmospheric heating anomalies over western Australia. El Niño provides an important forcing of the atmospheric circulation anomalies over the Ross Sea via inducing a Rossby wave train, and most surface melt events over the RIS happen during El Niño years. In addition, the anomalous atmospheric heating over western Australia, which is independent of El Niño, is another important forcing that triggers a Rossby wave train extending from subtropical Australia to the Ross Sea. The northerly flow toward the Ross Sea induces strong poleward moisture and heat transport, which further contributes to surface melt over the RIS.

SIGNIFICANCE STATEMENT: During austral summer, surface melt occurs over the Ross Ice Shelf, accelerates ice loss, and poses ice-sheet destabilization risks in a warming world. The northerly wind anomaly over the Ross sector provides strong poleward heat and moisture transport and is favorable for the surface melt. This wind anomaly is influenced by two remote forcings, El Niño and heating anomaly over western Australia, through generating Rossby wave trains from the tropics and subtropical Australia. This study reveals a previously unexplored relationship that atmospheric heating over western Australia influences large-scale circulation, contributing to surface melt.

KEYWORDS: Antarctica; ENSO; Heating; Rossby waves; Snowmelt/icemelt; Interannual variability

1. Introduction

The Ross Ice Shelf (RIS) is the largest cold-water ice shelf in Antarctica. Extensive floating ice shelves along the coast of Antarctica provide buttressing that impedes the glacier mass loss and stabilizes marine-ice-sheet grounding line (Dupont and Alley 2005; Gudmundsson 2013; The IMBIE Team 2018). Mass loss from the RIS has been increasing (DeConto and Pollard 2016; Baldacchino et al. 2022), and ice-shelf thinning and collapse have important implications on seaward ice flow enhancement, grounding-zone thinning, ice-sheet retreating, and sea level rise (Schoof 2007; DeConto and Pollard 2016). The dominant driver of ice mass loss from the RIS is through ocean-driven melt beneath the ice shelf (Stevens et al. 2020; Baldacchino et al. 2022), while surface melt observed over the RIS during summer could also weaken the stability of the ice shelf and further influence the grounded ice (Trusel et al. 2012; Baldacchino et al. 2022).

Numerous studies have reported high-impact summer surface melt events over the RIS and explained the local physical mechanisms responsible for these (Nicolas et al. 2017; Hu et al. 2019; Zou et al. 2021a,b). Marine air intrusions are observed to play an important role in these major melt events (Wille et al. 2019, 2021; Zou et al. 2021a; Li et al. 2023). The warm and moist air advection warms the coastal RIS directly and contributes to low-level liquid cloud formation (Nicolas et al. 2017; Scott et al. 2019). Enhanced cloud cover acts to increase the downward longwave radiation, which leads to the expansion of surface melt and dominates in most events (Hu et al. 2019; Li et al. 2023). In addition, when sufficient moisture is transported to topographic barriers by wind, the foehn effect can be the leading driver of melt under clear-sky conditions (Zou et al. 2019; Clem et al. 2022). Under strong foehn cases, foehn clearance and turbulent mixing increase downward shortwave radiation and sensible heat flux over the eastern RIS (Zou et al. 2019, 2021a,b).

The importance of persistent, intense high pressure blocking ridges in channeling anomalous poleward moisture toward

Denotes content that is immediately available upon publication as open access.

Supplemental information related to this paper is available at the Journals Online website: https://doi.org/10.1175/JCLI-D-23-0120.s1.

Corresponding author: Xiaoming Hu, huxm6@mail.sysu.edu.cn

DOI: 10.1175/JCLI-D-23-0120.1

RIS has been found in previous studies. Blocking can be influenced by various atmospheric drivers (Nicolas et al. 2017; Scott et al. 2019). One such driver in the Southern Hemisphere circulation is the Southern Annular Mode (SAM) which represents the strength of the circumpolar westerly wind (Rogers and Van Loon 1982; Gong and Wang 1999). During the negative phase of the SAM, weakened circumpolar westerlies and a shallow Amundsen Sea low create favorable conditions for frequent blocking over the South Pacific (Marshall et al. 2006, 2017). Additionally, the Pacific–South American teleconnections, two principal large-scale circulation patterns, exhibit a classic Rossby wave structure. Their largest geopotential height amplitude occurs over the South Pacific, with a prominent center reaching over the coast of West Antarctica, influencing regional climate dynamics (Mo and Higgins 1998).

The regional atmospheric circulation in the Ross and Amundsen Sea regions has also been reported to be modulated by tropical climate variability (Ding et al. 2012; Clem et al. 2020; Li et al. 2021; Chen et al. 2022; Orr et al. 2023). On decadal time scales, sea surface temperature (SST) variability associated with the interdecadal Pacific oscillation (IPO) and the Atlantic multidecadal oscillation (AMO) is a potential driver of multidecadal changes in Antarctic climate through low-frequency modulation of tropical–polar teleconnections (Simpkins et al. 2016). The South Pacific convergence zone (SPCZ) is also identified as a significant driver of the warming across the RIS at decadal scales (Clem et al. 2018, 2019). Specifically, they found that western tropical Pacific heating anomalies over the SPCZ are responsible for northerly flow to the Ross Ice Shelf for the austral spring season, but in the austral summer, the SPCZ forcing results in anticyclone circulations over the Ross Sea. Numerous studies have documented the significant influence of El Niño–Southern Oscillation (ENSO) on West Antarctica, including forcing interannual variability of the Amundsen Sea low (Ding and Steig 2013; Clem et al. 2017; Deb et al. 2018). Under a combination of El Niño and the negative phase of SAM, persistent, intense Amundsen Sea blocking highs are more likely to occur over the Ross sector (Fogt and Bromwich 2006; Tedesco 2009; Nicolas et al. 2017; Scott et al. 2019). Orr et al. (2023) considered a regional surface "melt potential" which describes the frequency and intensity of daily maximum temperature exceeding the melt threshold. They found that a strong signal comes from El Niño for the melt potential intensity but not for the melt potential frequency. This suggests other mechanisms may also play an important role for surface melt on the Ross Ice Shelf. Sun and Tan (2022) demonstrated that western North Pacific summer monsoon convection could affect synoptic-scale events remotely over the Antarctic at subseasonal time scale. The convective heating of the tropical atmosphere could generate stationary Rossby wave trains (Hoskins and Karoly 1981; Hoskins and Ambrizzi 1993; Fogt and Bromwich 2006; Yu et al. 2015) and strengthen the Hadley circulation and subtropical jet stream (Seager et al. 2003). The anomalous convergent flows at the descending branch of Hadley circulation act as a Rossby wave source exciting a wave train with alternating the centers of high pressure and low pressure around Antarctica. However, it is crucial to recognize that the propagation of Rossby wave depends on the background state to a large extent and the connection between tropical and Antarctic is relatively weak during austral summer (Jin and Kirtman 2009; Li et al. 2014, 2015a,b). Besides the large-scale circulation related to tropical Pacific SST/outgoing longwave radiation (OLR), local processes like the foehn effect and downward longwave radiation (Zou et al. 2021a; Li et al. 2023) play important roles in regulating surface melt events.

Motivated by the literature cited above, our study aims to identify remote forcings—such as SST anomalies associated with El Niño and other heating anomalies not related to ENSO—and their associated large-scale circulation patterns responsible for interannual variations in summer surface melt over the RIS. Our research focuses on the large-scale teleconnection pattern for the occurrence of long-lasting northerly wind anomalies over the RIS which is regarded as a favorable condition for the surface melt there. The paper is structured as follows. Section 2 provides an overview of the datasets, analysis methods, and model experiments. Section 3 examines the interannual variability of the summer surface melt over the RIS. The contributions of El Niño and western Australian rainfall to surface melt are discussed in section 4. Section 5 shows the results from model experiments. Finally, conclusions and a further discussion are given in section 6.

2. Data and methods

a. Datasets

This study analyzes the December–January means for the period of 1979–2021 because major surface melt often occurs at the peak of austral summer. The datasets used include 1) the monthly SST data from the Hadley Centre Sea Ice and Sea Surface Temperature (HadISST), version 1 (Rayner et al. 2003), in a 1° × 1° resolution; 2) the precipitation data from the Global Precipitation Climatology Project (GPCP) in a 2.5° × 2.5° resolution (Adler et al. 2003); 3) the monthly interpolated OLR from the National Oceanic and Atmospheric Administration (NOAA) in a 2.5° × 2.5° resolution (Liebmann and Smith 1996); 4) the winds and geopotential height from ERA5 released by the European Centre for Medium-Range Weather Forecasts in a 1° × 1° resolution (Hersbach et al. 2019); and 5) the daily Antarctic surface melt datasets produced by Picard and Fily (2006), which provides the daily status of melted or not melted for every pixel in a 25 × 25 km^2 resolution.

b. Analysis methods

The averaged SST anomalies over the Niño-3.4 region (170°–120°W, 5°S–5°N) are analyzed to measure ENSO variability. We employ the definition of ENSO events according to the NOAA's Climate Prediction Center based on a threshold of ±0.5 standard deviations. A commonly accepted melt index (MI) is employed to measure the melt strength in summer, with the melt area weighted by the duration of the melt (Liu et al. 2006; Nicolas et al. 2017). The MI is calculated as

$$\mathrm{MI} = A \cdot \sum_{i=1}^{n} m_i,$$

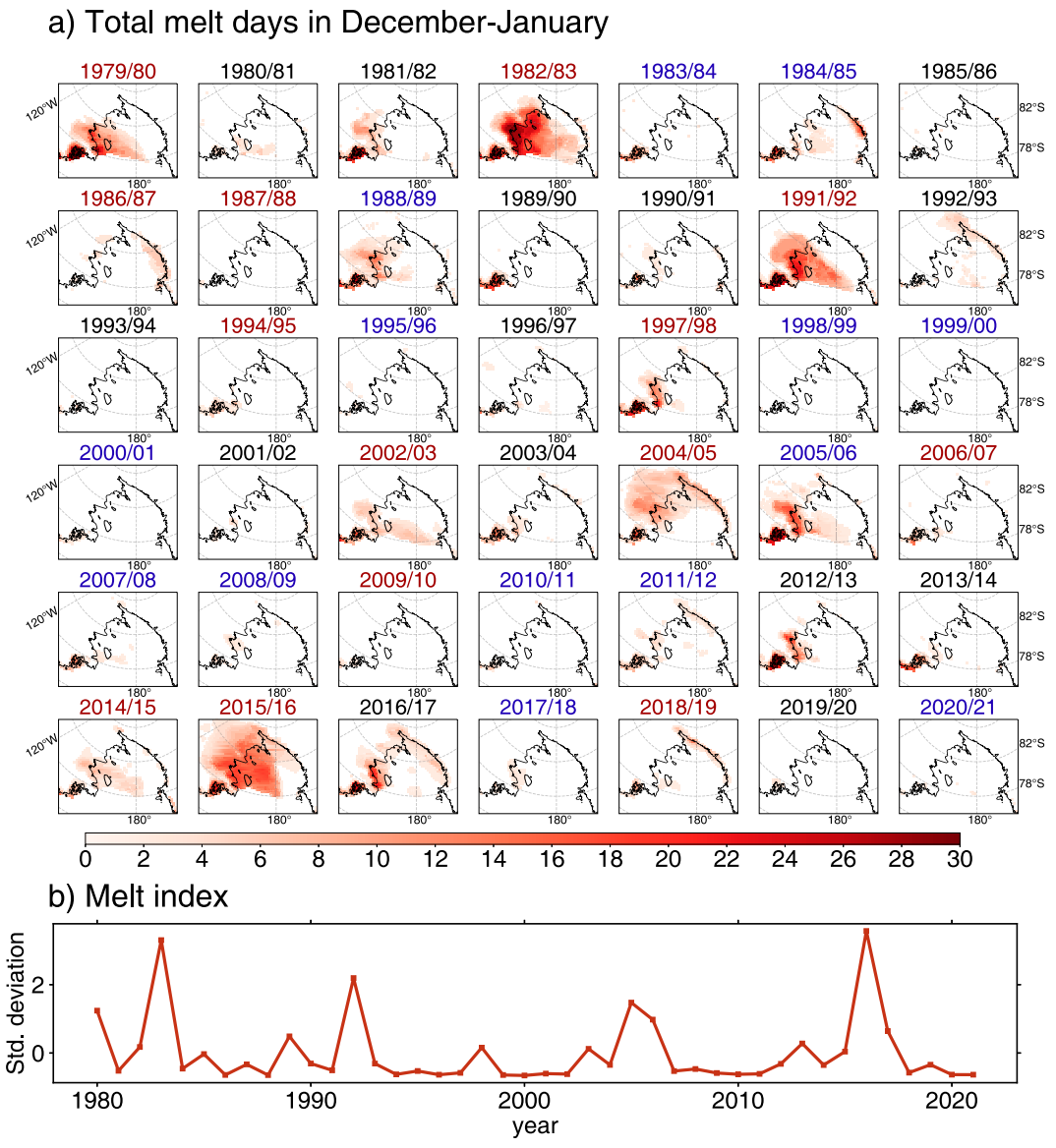

FIG. 1. Interannual variability of surface melt over the RIS in austral summer. (a) The total melt days in December–January (DJ) are retrieved from the passive microwave radiometer data (Torinesi et al. 2003; Picard and Fily 2006). The years colored in red and blue denote El Niño and La Niña years, respectively, according to the definition of the NOAA's Climate Prediction Center based on a threshold of ±0.5. (b) The time series of the normalized DJ MI for the Ross sector as shown in (a). The year corresponds to the month of January.

where A is the area of a pixel, m_i is the number of melt days during December and January for pixel i, and n is the number of pixels inside the Ross sector (Fig. 1a).

Correlation analysis is applied to evaluate relationship features. Partial correlation analysis (Abdi 2007) is also applied to involve the correlation between two variables while eliminating the influence of a third variable. Regression and partial regression are also employed. In this study, the influence of ENSO measured by the Niño-3.4 index is expected to be removed. For all analyses, the Student's t test is used to evaluate the statistical confidence levels of the results obtained.

Three types of diagnostic analyses that are complementary to each other are considered for gaining mechanism understanding of the wave train patterns identified from the correlation analysis. One is the wave activity flux (WAF), the so-called Plumb flux (Plumb 1985). Its direction is parallel to the group velocity of quasi-stationary Rossby waves, indicating the propagation of large-scale Rossby waves. In spherical coordinates,

$$\text{Plumb flux} = \frac{p\cos\varphi}{p_0}\begin{bmatrix} v'^2 - \dfrac{1}{(2\Omega a\sin 2\varphi)}\dfrac{\partial(v'\Phi')}{\partial\lambda} \\ -u'v' + \dfrac{1}{(2\Omega a\sin 2\varphi)}\dfrac{\partial(u'\Phi)}{\partial\lambda} \end{bmatrix},$$

where φ and λ are the latitude and longitude coordinates; p denotes pressure; $p_0 = 1000$ mb; u', v', and Φ' represent the

TABLE 1. Description of model design and experiments.

Name	Abbreviations	Description
Ctrl run	CTRL	Climatological mean global SST with seasonal cycle, for the period 1981–2010 obtained from HadISST
Western Australia heating run	WA_HEATING	Climatological mean global SST + strengthened the convective heating over western Australia (105°–135°E/20°–40°S)
Whole topical SST warming run	WT_HEATING	Climatological mean global SST + whole tropical SST warming (15°N–15°S)

stationary disturbance of zonal wind, meridional wind, and geopotential height obtained by removing the zonal mean; and a and Ω are the radius and rotation rate of Earth. The other two irrotational winds and Rossby wave sources are defined as the convergence of vorticity fluxes by irrotational winds, following Sardeshmukh and Hoskin (1988).

In all calculations for geopotential height, the zonal mean is subtracted. Note that for austral summer, December and January (DJ), the year corresponds to January.

c. *Model description*

The model used in this study is the Community Atmosphere Model, version 4 (CAM4), the atmospheric component of the Community Earth System Model, version 1.2.2, from the National Center for Atmospheric Research (NCAR; Neale et al. 2013), with a horizontal resolution of 1.9° × 2.5° and 26 levels in a hybrid pressure sigma coordinate. The simulations are implemented by the F component setting, meaning that the ocean model is a prescribed data component and the surface boundary forcing dataset is a merged product based on monthly mean SST and sea ice concentration.

This study is mainly based on three model experiments. The control experiment, referred to as CTRL, is forced by the monthly mean global SST from 1981 to 2000. Three sensitivity experiments are conducted with all settings identical to those of the CTRL except that anomalous forcing is imposed over western Australia and the tropics during DJ, referred to as western Australia heating run (WA_HEATING) and whole topical SST warming run (WT_HEATING) experiments, respectively. The design of experiments is briefly described in Table 1. All experiments have been integrated for 35 years, and the outputs from years 6–35 are analyzed.

In the WA_HEATING run, we change the convective heating by imposing an amplification factor based on the algorithm of bilinear decline in each time step of model integration in austral summer. Western Australian heating forcing due to the strengthened rainfall is added to the key region of 105°–135°E/20°–40°S. The WT_HEATING run is conducted to demonstrate the influence of whole tropical SST warming. An additional SST perturbation is obtained from the composite SST anomalies for the years that the normalized DJ-mean Niño-3.4 index is over the threshold of 0.5 standard deviation. Only the SSTs across the tropics (15°N–15°S) during December and January are perturbed. The atmosphere in other regions is forced by the monthly climatology mean SST and sea ice as in the CTRL run.

3. Interannual variability of summer surface melt of the RIS

The total melt days in December and January each year for 1979–2021 (Fig. 1a) indicate that during austral summer surface melt occurs over the RIS. The persistent melt above 20 days is mainly located over the eastern RIS. To depict the significance of the melt, we use a normalized MI calculated for the RIS. Five of seven years in which the normalized MI exceeds 0.5 occur in El Niño years suggests that the largest-extent and longest-lasting melt events often coincide with El Niño events, consistent with previous studies (Nicolas et al. 2017; Scott et al. 2019). As shown in Fig. 1b, the RIS summer surface melt exhibits remarkable interannual variations, and several extreme events are spotted. High MI values were identified as major surface melt events in previous studies, as in 1983, 1992, 2005, and 2016. These events often occur in conjunction with direct warm and moist air intrusions from the Ross Sea (Li et al. 2023). The marine advection warms the coastal RIS and promotes the formation of clouds which affects surface energy balance and favors the expansion of the melt (Hu et al. 2019; Zou et al. 2021a,b). When modified by the rugged topography of Marie Byrd Land, the warm marine intrusions may lead to temperature increases on the lee side of a mountain ridge (Zou et al. 2019). Since the poleward wind anomaly has been proven to be important for individual surface melt cases, we will further explore whether it is equally important for the interannual variability of surface melt.

The correlation map between normalized MI and DJ-mean 850-hPa poleward meridional wind anomalies shows that surface melt is significantly correlated with northerly flow over the Ross Sea that favors strong heat transport from the lower latitudes to the RIS (Fig. 2a). The correlation between MI and integrated vapor transport from 900 to 300 hPa was also examined (Fig. S1 in the online supplemental material). The results are in close agreement with those obtained from the meridional wind. However, the significant areas of correlation are more restricted and occur predominantly at higher latitudes, supporting the fact that an increase in wind speed corresponds to an increase in water vapor and heat transport. We construct an index to facilitate the measurement of northerly wind intensity. This northerly flow index (nVa) is

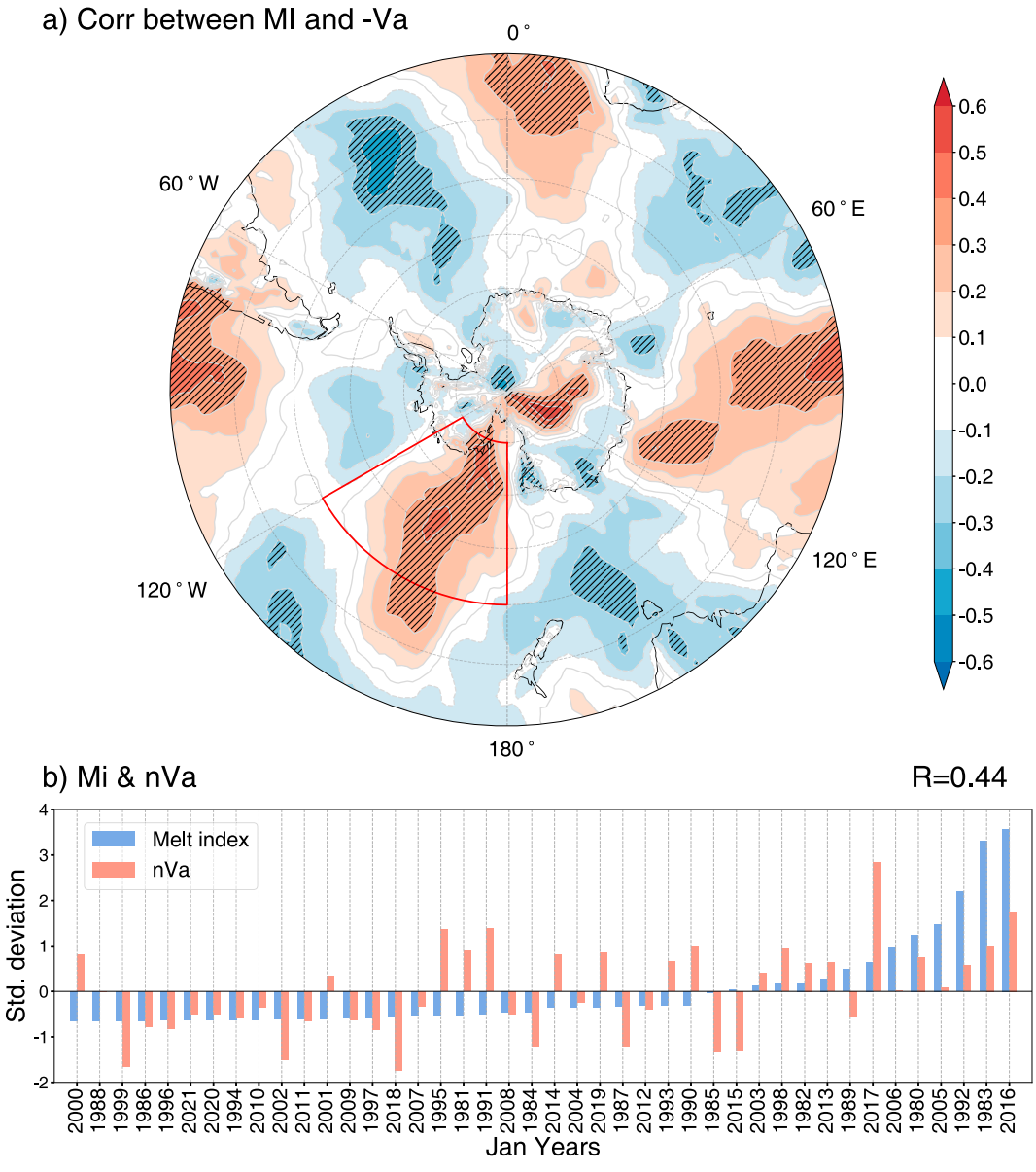

FIG. 2. (a) Correlation between normalized MI and DJ-mean 850-hPa poleward meridional wind anomalies. Black slashes indicate the correlation coefficients significantly exceeding the 95% confidence level. (b) 1980–2021 normalized MI and area-averaged poleward meridional wind anomalies (nVa). The boundaries of area-averaged meridional wind anomalies are outlined in (a) in the red line (50°–80°S, 180°–120°W). In (b), the years are ranked from the lowest MI to the highest MI.

defined as the time series of average DJ-negative 850-hPa meridional wind anomalies over the region of maximum correlation (180°–120°W, 50°–80°S). As shown in Fig. 2b, in which the normalized MI and nVa index are ranked from the lowest MI to the highest MI, more melt tends to occur with a prevalent northerly wind anomaly. The correlation between MI and nVa index reaches 0.44. Given the complex local air–ice–topography interaction, the intensity of northerly wind anomaly and melt strength are not highly consistent. To focus on the atmospheric large-scale circulation, we use the nVa index to identify the background circulation pattern favorable to surface melt over the RIS.

4. Contributions of El Niño and western Australian heating

Figure 3 shows the correlation of the nVa index with geopotential height and wind fields at 200 hPa (Fig. 3a) and 850 hPa (Fig. 3b). The profound feature is wave trains emanating from the tropics marked with dark red arrows in Fig. 3a. The wave train originating from the central tropical

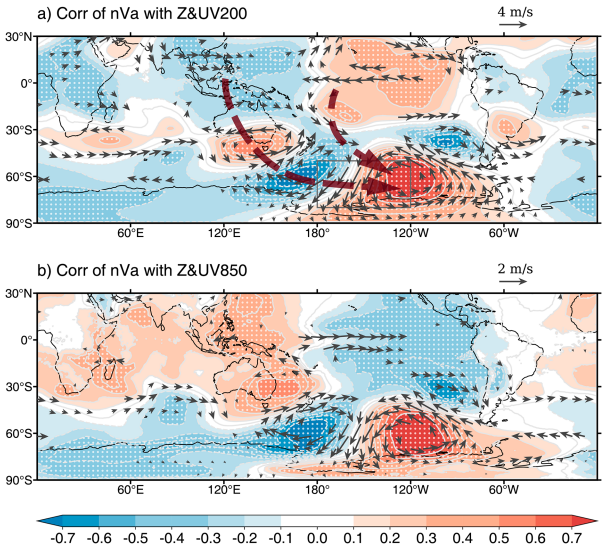

FIG. 3. Correlation of normalized nVa index with DJ-mean geopotential height (shadings) and regression of normalized nVa index on horizontal wind (vectors) anomalies at (a) 200- and (b) 850-hPa levels. The white dots denote the significant correlation coefficients above the 95% confidence level. The vectors that are significantly above the 95% confidence level (either zonal or meridional) are shown. The gray box in (a) indicates the calculated area for the nVa index.

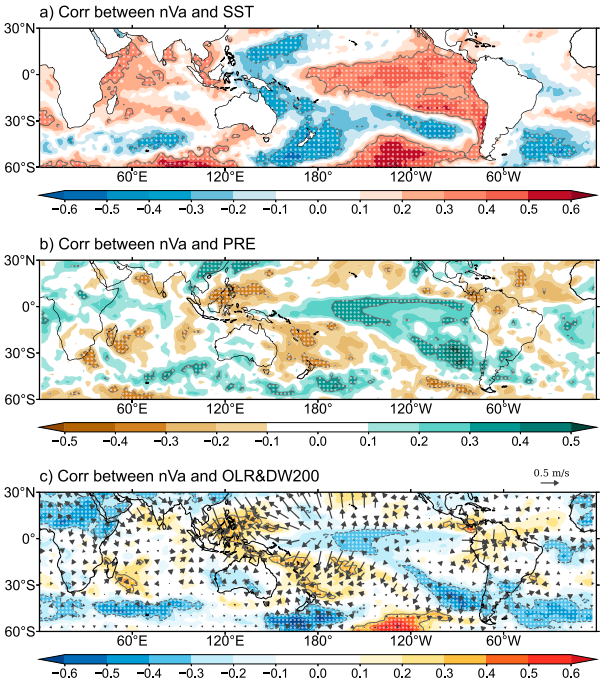

FIG. 4. Correlation between normalized nVa index and (a) SST, (b) precipitation, and (c) OLR anomalies in austral summer (shadings). The vectors in (c) indicate the regression of normalized nVa index on divergent wind at 200 hPa. The white dots denote the correlation coefficients significantly above the 95% confidence level.

Pacific follows a "great circle" path, and the vertical response of geopotential height anomalies is baroclinic in the tropics but barotropic elsewhere (Gill 1980). There is also an indication of a barotropic wave train emanating from the Maritime Continent toward West Antarctica. The low and high geopotential height anomalies over the Pacific sector of the Southern Ocean induce northerly flow over the Ross Sea, favorable for warm and moist marine air intrusion into the RIS.

The correlation between SST and nVa index in Fig. 4a suggests that the variability of northerly wind over the RIS is associated with the SSTs of the tropical Pacific and northern Indian Oceans, and the SST correlation in the tropic structures the characteristic of El Niño events. Accompanied by enhanced rainfall (Fig. 4b) and reduced OLR (Fig. 4c), the warming of SST in the tropical central Pacific can induce anomalous convection and Rossby wave source (RWS) in the tropics (Fig. S2). The anomalous divergence over the central Pacific and anomalous convergence over the Maritime Continent serve as sources for the formation of Rossby wave trains (Fig. 4c). This feature is consistent with the previous results that ENSO-induced upper-level divergence associated with anomalous rainfall acts as a Rossby wave source and excites equivalent barotropic Rossby wave trains (Yu et al. 2015; Ding and Steig 2013). ENSO-related SST anomalies also drive changes in the climatological Walker circulation and further promote anomalous descending motion over the Maritime Continent (Cai et al. 2020). Divergence anomalies due to suppressed convection over the Maritime Continent region can also act as effective Rossby wave sources and excite a Rossby wave train propagating into the Southern Hemisphere (Sardeshmukh and Hoskin 1988; Cai et al. 2011). Anomalous warming in the Indian Ocean is also displayed in Fig. 4a, and it may be related to the forcing from the Pacific (Klein et al. 1999). In the mid–high latitude, the negative geopotential height anomaly center corresponds to negative SST anomaly, positive precipitation, and negative OLR anomaly, while positive height anomaly can induce the opposite pattern. These relationships indicate that the SST features are forced by anomalous atmospheric circulation and show spatial distributions resembling the teleconnection pattern of these Rossby waves.

The propagation of the wave train is further illustrated by the associated stationary WAF, computed according to Plumb (1985). It can be seen from Fig. 5 that a prominent arc-shaped stream of WAF propagates away from the south of Australia toward the Ross Sea and the Amundsen Sea and returns to South America. With enhancement as propagating southward, the largest WAF appears over the Pacific sector of the Southern Ocean.

El Niño provides an important forcing of the anomalous blocking high over the 150°–90°W sector of the Southern Ocean, leading to strong poleward warm marine air advection toward the RIS. Although prior studies have highlighted the influence of ENSO-related teleconnection in West Antarctic climate variability, the tropical teleconnection is relatively weak during austral summer (Li et al. 2015a, 2021) and the northerly wind cannot be fully explained by tropical variability. As discussed in Fig. 1, the four strongest surface melt

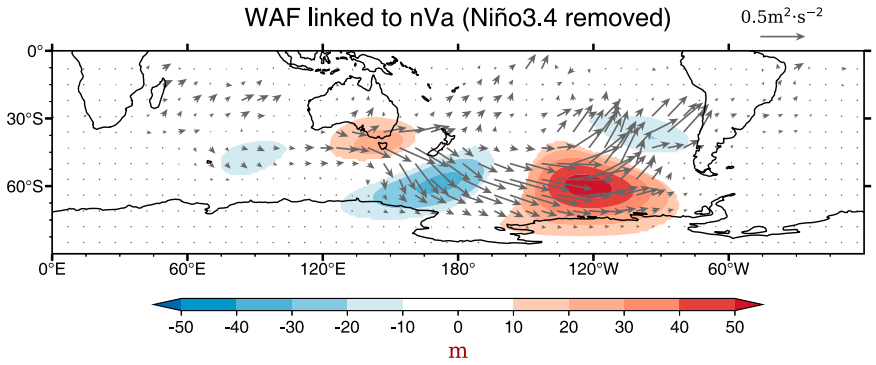

FIG. 5. Regression of 200-hPa geopotential height anomalies (shading; m) and WAF (vectors) on the normalized nVa index. Shading denotes the regions where correlation is significant at the 95% confidence level. Wavevectors with both zonal and meridional components smaller than 0.05 $m^2 s^{-2}$ are omitted.

events occur during peak El Niño winter, while surface melt events may also happen during peak La Niña winter.

What is the other forcing that may regulate the interannual variability of the northerly wind over the RIS? We use the Niño-3.4 index to indicate the tropical Pacific forcing. Figure 6 depicts the partial correlation of the nVa index with geopotential height and winds after removing the influence of ENSO. The geopotential height anomalies mostly disappear in the tropics; however, it is still prominent that the wave train propagates away from subtropical Australia toward

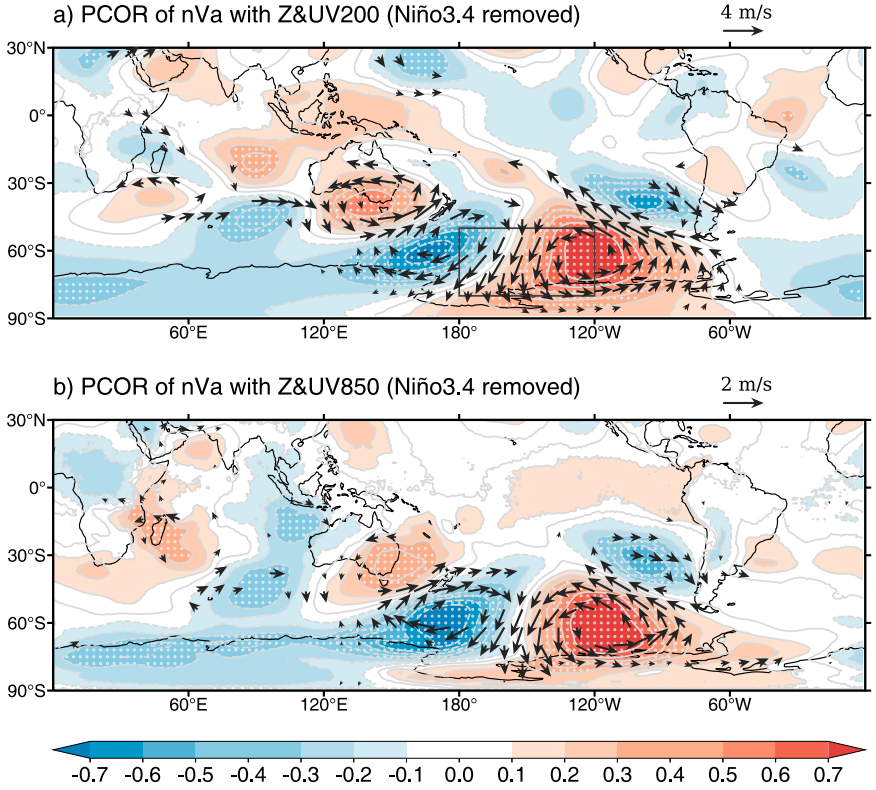

FIG. 6. Partial correlation of normalized nVa index with DJ-mean geopotential height (shadings) and partial regression of normalized nVa index on horizontal wind (vectors) anomalies by removing the normalized DJ Niño-3.4 index, at (a) 200-hPa and (b) 850-hPa levels. The white dots denote the significant correlation coefficients above the 95% confidence level. The vectors that are significantly above the 95% confidence level (either zonal or meridional components) are shown. The gray box in (a) indicates the calculated area for the nVa index.

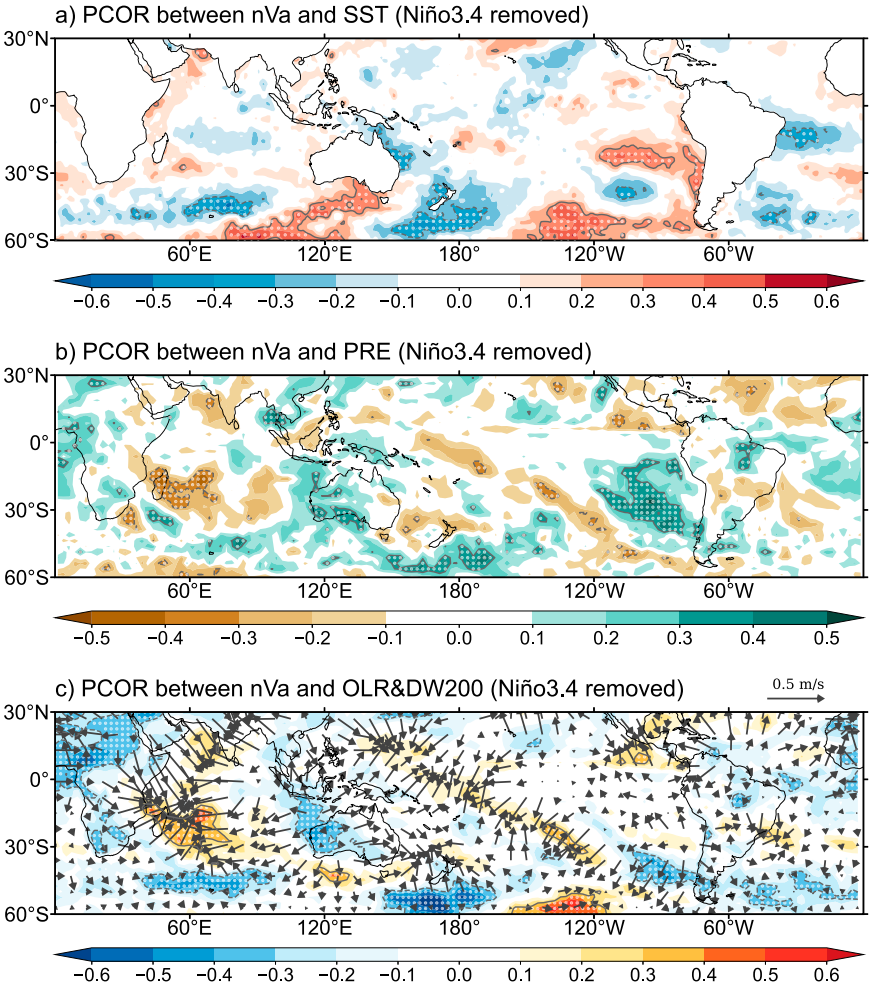

FIG. 7. Partial correlation between normalized nVa index and (a) SST, (b) precipitation, and (c) OLR anomalies by removing the normalized DJ Niño-3.4 index (shadings). The vectors in (c) indicate the partial regression of normalized nVa index on divergent wind at 200 hPa by removing the normalized DJ Niño-3.4 index. The white dots denote the correlation coefficients significantly above the 95% confidence level.

West Antarctica and returns to South America, suggesting that the wave train is independent of ENSO-related teleconnection to a certain degree.

We now examine the relationship between SST and nVa index with the Niño-3.4 index removed. The pattern is significantly different from the original result in Fig. 4a. The SST warming in both tropical Pacific and northern Indian Oceans disappears completely (Fig. 7a), which supports that the ENSO-induced Pacific SST anomalies are capable of modulating the SST changes in the Indian Ocean (Fig. 3a). Meanwhile, Fig. 7 reveals that the nVa index is positively correlated with the strengthened rainfall and negative OLR anomaly over western Australia when the influence of ENSO is removed.

The anomalous divergent winds and positive RWS anomaly over western Australia also indicate that the rainfall accompanied by atmospheric deep convective heating may play a key role in driving the stationary Rossby wave (Fig. 7c and Fig. S3). As confirmed by WAF (Fig. 8), this heating over western Australia induces anticyclonic anomalies in the upper troposphere and generates a Rossby wave train propagating southeastward. The barotropic Rossby wave response favors a blocking condition and maintains the northerly wind over the Ross sector.

We define a rainfall index as the area-mean DJ rainfall anomalies over western Australia (115°–135°E, 20°–40°S) to examine the influence of atmospheric heating. The partial correlation of normalized nVa index with DJ-mean geopotential height and horizontal wind anomalies by removing the normalized rainfall index shows that the two wave trains are still prominent (Fig. S4). In addition, the wave train from the Maritime Continent becomes stronger after removing the influence of western Australian atmospheric heating (Fig. S5). The results discussed here and in the above sections suggest that El Niño and the western Australian atmospheric heating

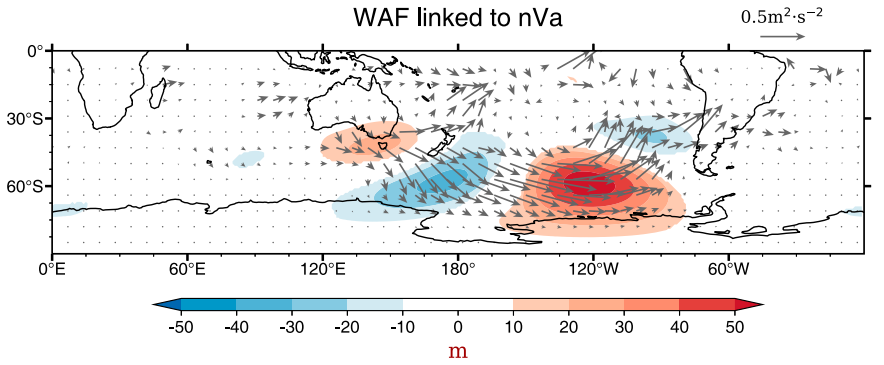

FIG. 8. Partial regression of 200-hPa geopotential height anomalies (shading; m) and WAF (vectors) on normalized nVa index by removing the normalized DJ Niño-3.4 index. Shading denotes the regions where the correlation is significantly above the 95% confidence level. Wave-vectors with both zonal and meridional components smaller than 0.05 $m^2\ s^{-2}$ are omitted.

regulate the interannual variability of surface melt over the RIS through modulating local prevalent northerly wind.

5. Model simulations forced by tropical Pacific SST and deep convective heating over western Australia

To support the above results that strengthened northerly wind over the RIS is primarily owing to the high-latitude atmospheric circulation response to tropical SST warming and western Australian deep convection heating, we use the state-of-the-art atmospheric model CAM4 to simulate this inferred causal relationship. The detailed description of the experiment design is presented in section 2.

In the WA_HEATING run, the heating is intensified over the key region of 105°–135°E/20°–40°S and the center is at 30°S, 120°E (Fig. 9a). We select the heating center according to the correlation results between nVa and precipitation (Fig. 7b). Given that the maximum anomalous rainfall over western Australia is about 3 mm day^{-1} (Fig. S6), the latent heat released by precipitation of 3 mm day^{-1} is equivalent to a column average heating of 0.75 K day^{-1} (Jin and Hoskins 1995). Diabatic heating anomalies with maximum heating of

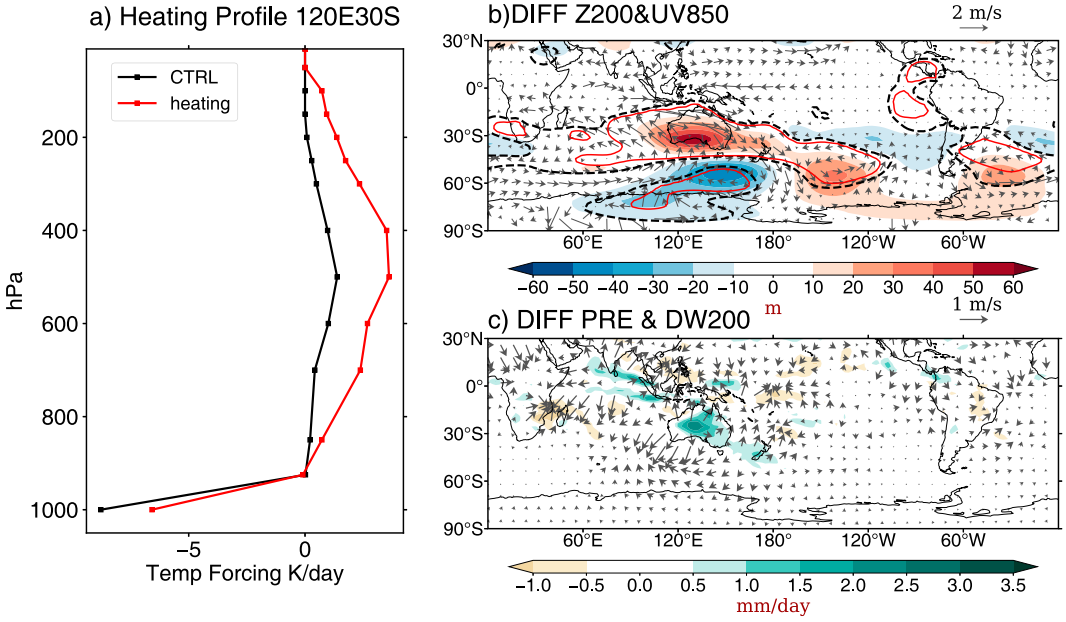

FIG. 9. Response of the CAM4 to anomalous heating over western Australia in austral summer (DJ). (a) DJ convective heating profiles (K day^{-1}) over the heating center (30°S, 120°E) in CTRL and WA_HEATING experiments. The black and red lines are for CTRL and WA_HEATING experiments, respectively. (b) Differences in 200-hPa geopotential height (shading; m) and 850-hPa horizontal winds (vectors; m s^{-1}) between WA_HEATING and CTRL. The red and black contour lines denote 95% and 90% significant confidence levels. (c) Differences in precipitation (shading; mm day^{-1}) and 200-hPa divergent wind (vectors; m s^{-1}) between WA_HEATING and CTRL.

3 K day^{-1} at σ = 0.45 (Fig. 9a; red line) are imposed over western Australia. The distribution of heating profiles in the CTRL is consistent with that in previous studies (Zhang and McFarlane 1995). The difference in the simulation results between the WA_HEATING and the control run represents the model response to deep convective heating associated with western Australian rainfall. The model response of 200-hPa geopotential height and 850-hPa winds is very similar to the partial correlation result: Enhanced heating lifts the geopotential height in the upper troposphere locally and then the anomalous strong divergence and positive RWS anomaly in the upper level generate stationary Rossby wave train (Fig. 9 and Fig. S7). The WAF can also be observed that the wave train originating from subtropical Australia propagates southward and eastward in model simulations (Fig. S8). The cyclone–anticyclone pair over the Pacific sector of the Southern Ocean is highly barotropic, and the strong anomalous northerly wind over the RIS in the lower troposphere is manifested by this associated cyclone–anticyclone pair. The increased rainfall over Australia is consistent with the enhanced deep convection as expected (Fig. 9c). The model simulation well captures the key element of this teleconnection pattern in reanalysis data. Additionally, we conduct another three sensitivity experiments with the heating center located further east at 30°S, 125°E (Fig. S9), further west and south at 30°S, 110°E (Fig. S10), and a stronger heating experiment with a maximum heating of 4 K day^{-1}, whereas the WA_HEATING run uses 3 K day^{-1} (Fig. S11). The pattern of wave trains from the tropics and Australia toward West Antarctica remains consistent, although the magnitude of geopotential response varies. The finding indicates that wave train responses are not strongly sensitive to the region of heating forcing and the responses increase with forcing strength. Due to the observed negative partial correlation between the nVa index and OLR over the western Indian Ocean, we have conducted an experiment forced by anomalous atmospheric cooling (Fig. S12). The cooling over the western Indian Ocean triggers geopotential height anomalies over the Southern Hemisphere, but the response is relatively weaker and is mainly confined to the midlatitudes compared to the previous experiments. This further suggests that the anomalous atmospheric heating over western Australia is a significant forcing that triggers the Rossby wave toward West Antarctica.

Given that ENSO induces SST changes in other basins as shown in section 4, we perform the WT_HEATING run by using the same climatological SSTs, augmented by the anomalous SST pattern observed across the tropics in Fig. 10a during December and January. The additional SST perturbation is obtained from the composite SST anomalies for the years that the DJ-mean Niño-3.4 index is over the threshold of 0.5. Figure 10b depicts the differences in 200-hPa geopotential height and 850-hP winds between WT_HEATING and CTRL. In response to the SST forcing across the tropics, this experiment produces the circulation pattern in which both the wave train from central Pacific and the wave train emanating from the Maritime Continent toward West Antarctica are displayed. The El Niño–related SST warming in the tropical central–eastern Pacific induces an anomalous tropical Walker

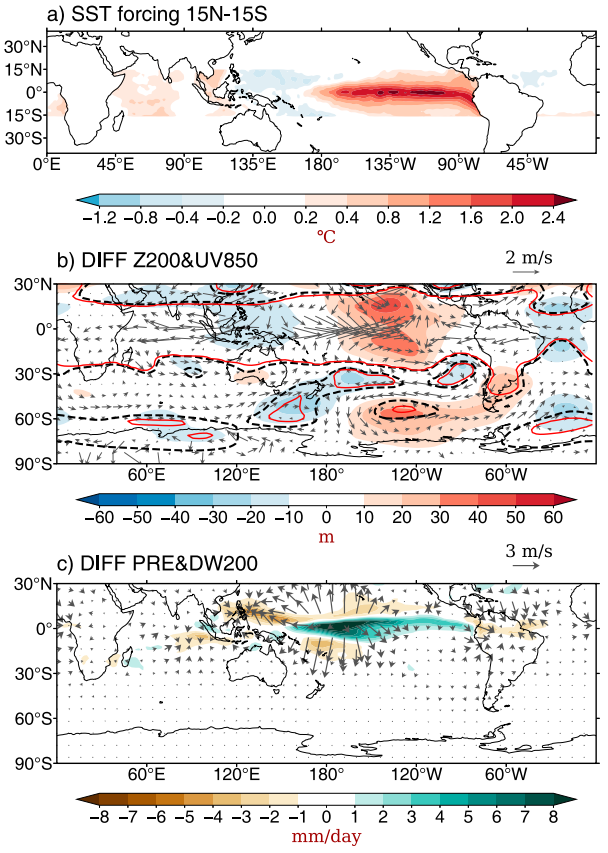

FIG. 10. Response of the CAM4 to anomalous warm SST in austral summer (DJ). (a) Spatial pattern of anomalous SST forcing (shading; °C) in WT_HEATING experiment in December. (b) Differences in 200-hPa geopotential height (shading; m) and 850-hPa horizontal winds (vectors; m s^{-1}) between WT_HEATING and CTRL. The red and black contour lines denote 95% and 90% significant confidence levels. (c) Differences in precipitation (shading; mm day^{-1}) and 200-hPa divergent wind (vectors; m s^{-1}) between WT_HEATING and CTRL.

circulation with upward motion anomalies over the tropical central Pacific and downward motion anomalies around the Maritime Continent (Fig. 11b). The accompanied upper-level divergence and RWS anomalies around the tropical central Pacific and upper-level convergences and RWS anomalies around the Maritime Continent could be considered as effective Rossby wave sources for the formation of the Rossby wave train from the tropics toward west Antarctica (Figs. 10c and 11a, Figs. S13 and S14), which is consistent with previous studies (Sardeshmukh and Hoskin 1988; Cai et al. 2011, 2020). Forced by tropical variability, the geopotential height fluctuations are larger in the tropics than in the higher latitudes. Compared with the Rossby wave response in WA_HEATING (Fig. 9b), the cyclone–anticyclone pair does not extend southward and the maximum of the northerly wind over the Sothern Pacific is in the midlatitudes. El Niño tends to induce prominently enhanced rainfall in the central Pacific and reduced rainfall in the eastern Indian Ocean in model simulations (Fig. 10c).

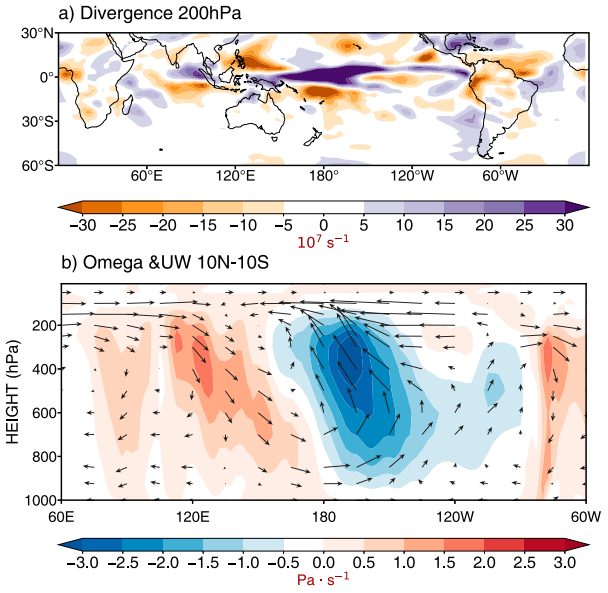

FIG. 11. Mechanism analysis and diagnosis of atmospheric anomalies in model experiments. Differences in DJ (a) 200-hPa divergence (shading; s^{-1}) and (b) zonal (10°N–10°S mean) vertical circulation (shading; Pa s^{-1}) between WT_HEATING and CTRL. The vectors indicate the directions of zonal and vertical winds.

The strong coherence between observational analyses and model responses shows that El Niño and strengthened atmospheric heating due to western Australian rainfall are identified as two major independent remote forcings that generate Rossby waves toward West Antarctica.

6. Conclusions and discussion

This study focuses on remote forcing to regulate the interannual variability of major melt events over the RIS during austral summer. We utilize a commonly accepted melt index (MI), defined as the total number of melt days for the melt pixels during the austral summer, to quantify the interannual variability of surface melt strength. Our results have significant implications for understanding the role of large-scale atmospheric circulation in driving the interannual variability of surface melt. The correlation between MI and poleward meridional wind shows surface melt is frequently associated with the anomalous northerly warm and moist air advection over the Ross Sea sector. We define an index based on the area-average northerly wind over 50°–80°S/120°–180°W to measure the intensity of poleward winds, and this nVa index is significantly correlated with the MI.

The main finding of this study is that the El Niño–related SST anomalies in the tropical central–eastern and the atmospheric heating anomaly over western Australia are two important factors for the generation of the Rossby wave trains toward West Antarctica (Fig. 12), leading to the development of northerly wind anomalies over the RIS which is favorable condition for major ice melt events. Associated with El Niño–related SST anomalies in the tropical Pacific are two distinct wave trains toward West Antarctica, one from the central Pacific and the other from the Maritime Continent. On the other hand, the atmospheric heating associated with positive rainfall anomalies over western Australia, which is independent of El Niño, is also identified as a forcing of the atmospheric wave train propagating away from subtropical Australia toward the Ross Sea and returning northward over South America.

The CAM4 simulations confirm that these observed wave trains are a consequence of the circulation changes driven by El Niño and western Australian heating. They work as two independent forcings triggering wave trains and make the teleconnection pattern extending to the higher latitudes around West Antarctica and regulating the interannual variability of northerly wind anomalies over the Ross sector.

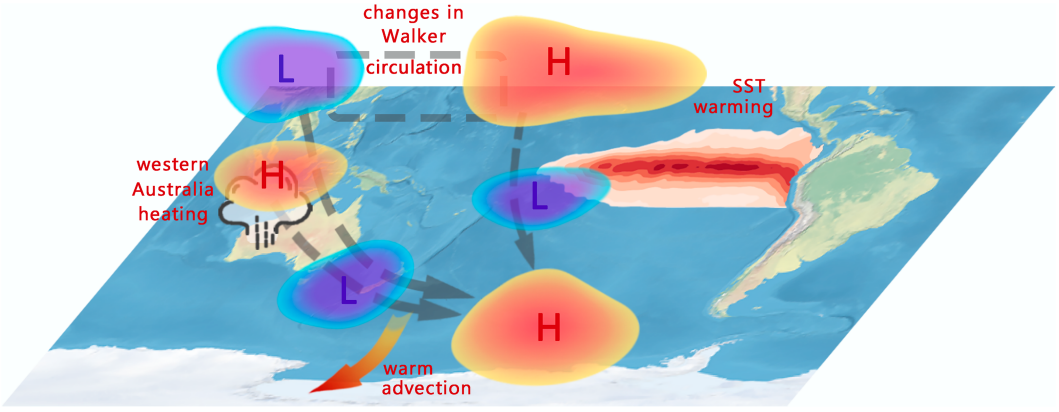

FIG. 12. Schematic figure of the remote forcing for the circulation pattern favorable to surface melt over the RIS. The El Niño–related SST variability generates two wave trains toward West Antarctica. One wave train originates directly from the central Pacific, while the other emanates from the Maritime Continent, driven by the anomalous descending motion from El Niño–induced changes in Walker circulation. Anomalous atmospheric heating over western Australia induces anticyclonic anomalies in the upper troposphere and generates a Rossby wave train propagating southeastward. The anomalous high and low pressure centers over West Antarctica lead to northerly wind over the Ross sector providing warm advection favorable to surface melt.

Our results complement the findings of Clem et al. (2018, 2019) who link the northerly flow/anticyclone circulation pattern over the RIS in austral spring/summer seasons to western tropical Pacific heating anomalies over the SPCZ for the decadal variability of RIS's surface melt. We here identify tropical heating anomalies over the eastern tropical Pacific (i.e., El Niño) and over western Australia are responsible for the interannual variability of the northerly flow to the RIS in austral summer, which plays an important role for the interannual variability of RIS's surface melt.

In addition, after the removal of the ENSO signal, an anomalous center of negative precipitation emerges over the western Indian Ocean (Fig. 4b), but there is no corresponding SST change. We have added an anomalous atmospheric cooling over the western Indian Ocean in model simulation (Fig. S12a). Although the geopotential height anomalies in response to the anomalous Indian Ocean cooling are relatively weak and are primarily confined to the midlatitudes (Fig. S12), they could strengthen the extratropical signal from El Niño and western Australian heating. The possible influence from the Indian Ocean deserves further investigation. The interannual variability of the austral summer Rossby wave source exhibits an active region to the east of Australia (Ding et al. 2012), which is close to the major forcing due to strengthened rainfall discussed in this study. Therefore, the role of internal variability in generating the wave train is desired to be further investigated.

Although major melt events and their associated local physical processes have been discussed in previous studies (Nicolas et al. 2017; Hu et al. 2019; Zou et al. 2021a,b), our results provide an enhanced understanding of large-scale circulation favorable for surface melt over the RIS through the northerly wind and its remote forcings.

Acknowledgments. The authors thank the Editor Dr. Tomoki Tozuka and four anonymous reviewers for their valuable comments which helped greatly to improve the manuscript. This study was supported by the National Natural Science Foundation of China (Grant 42075028), the Guangdong Province Key Laboratory for Climate Change and Natural Disaster Studies (Grant 2020B1212060025), and the Southern Marine Science and Engineering Guangdong Laboratory (Zhuhai) (Grant SML2021SP302).

Data availability statement. The HadISST dataset was downloaded from the Met Office (UKMO) at https://www.metoffice.gov.uk, the ERA5 at https://www.ecmwf.int/en/forecasts/datasets/reanalysis-datasets/era5, the OLR at https://psl.noaa.gov/data/gridded/data.olrcdr.interp.html, and the GPCP at https://psl.noaa.gov/data/gridded/. The daily Antarctic surface melt dataset was obtained at https://snow.univ-grenoble-alpes.fr/melting/.

REFERENCES

Abdi, H., 2007: Part (semi partial) and partial regression coefficients. *Encyclopedia of Measurement Statistics*, N. Salkind, Ed., Sage Publications, 736–739.

Adler, R. F., and Coauthors, 2003: The version-2 Global Precipitation Climatology Project (GPCP) monthly precipitation analysis (1979–present). *J. Hydrometeor.*, **4**, 1147–1167, https://doi.org/10.1175/1525-7541(2003)004<1147:TVGPCP>2.0.CO;2.

Baldacchino, F., M. Morlighem, N. R. Golledge, H. Horgan, and A. Malyarenko, 2022: Sensitivity of the Ross Ice Shelf to environmental and glaciological controls. *Cryosphere*, **16**, 3723–3738, https://doi.org/10.5194/tc-16-3723-2022.

Cai, W., P. van Rensch, T. Cowan, and H. H. Hendon, 2011: Teleconnection pathways of ENSO and the IOD and the mechanisms for impacts on Australian rainfall. *J. Climate*, **24**, 3910–3923, https://doi.org/10.1175/2011JCLI4129.1.

——, and Coauthors, 2020: Climate impacts of the El Niño–Southern Oscillation on South America. *Nat. Rev. Earth Environ.*, **1**, 215–231, https://doi.org/10.1038/s43017-020-0040-3.

Chen, J., X. Hu, S. Yang, S. Lin, and Z. Li, 2022: Influence of convective heating over the Maritime Continent on the West Antarctic climate. *Geophys. Res. Lett.*, **49**, e2021GL097322, https://doi.org/10.1029/2021GL097322.

Clem, K. R., J. A. Renwick, and J. McGregor, 2017: Large-scale forcing of the Amundsen Sea low and its influence on sea ice and West Antarctic temperature. *J. Climate*, **30**, 8405–8424, https://doi.org/10.1175/JCLI-D-16-0891.1.

——, A. Orr, and J. O. Pope, 2018: The springtime influence of natural tropical Pacific variability on the surface climate of the Ross Ice Shelf, West Antarctica: Implications for ice shelf thinning. *Sci. Rep.*, **8**, 11983, https://doi.org/10.1038/s41598-018-30496-5.

——, B. R. Lintner, A. J. Broccoli, and J. R. Miller, 2019: Role of the South Pacific convergence zone in West Antarctic decadal climate variability. *Geophys. Res. Lett.*, **46**, 6900–6909, https://doi.org/10.1029/2019GL082108.

——, R. L. Fogt, J. Turner, B. R. Lintner, G. J. Marshall, J. R. Miller, and J. A. Renwick, 2020: Record warming at the South Pole during the past three decades. *Nat. Climate Change*, **10**, 762–770, https://doi.org/10.1038/s41558-020-0815-z.

——, D. Bozkurt, D. Kennett, J. C. King, and J. Turner, 2022: Central tropical Pacific convection drives extreme high temperatures and surface melt on the Larsen C Ice Shelf, Antarctic Peninsula. *Nat. Commun.*, **13**, 3906, https://doi.org/10.1038/s41467-022-31119-4.

Deb, P., A. Orr, D. H. Bromwich, J. P. Nicholas, J. Turner, and J. S. Hosking, 2018: Summer drivers of atmospheric variability affecting ice shelf thinning in the Amundsen Sea Embayment, West Antarctica. *Geophys. Res. Lett.*, **45**, 4124–4133, https://doi.org/10.1029/2018GL077092.

DeConto, R. M., and D. Pollard, 2016: Contribution of Antarctica to past and future sea-level rise. *Nature*, **531**, 591–597, https://doi.org/10.1038/nature17145.

Ding, Q., and E. J. Steig, 2013: Temperature change on the Antarctic Peninsula linked to the tropical Pacific. *J. Climate*, **26**, 7570–7585, https://doi.org/10.1175/JCLI-D-12-00729.1.

——, ——, D. S. Battisti, and J. M. Wallace, 2012: Influence of the tropics on the Southern Annular Mode. *J. Climate*, **25**, 6330–6348, https://doi.org/10.1175/JCLI-D-11-00523.1.

Dupont, T. K., and R. B. Alley, 2005: Assessment of the importance of ice-shelf buttressing to ice-sheet flow. *Geophys. Res. Lett.*, **32**, L04503, https://doi.org/10.1029/2004GL022024.

Fogt, R. L., and D. H. Bromwich, 2006: Decadal variability of the ENSO teleconnection to the high-latitude South Pacific governed by coupling with the Southern Annular mode. *J. Climate*, **19**, 979–997, https://doi.org/10.1175/JCLI3671.1.

Gill, A. E., 1980: Some simple solutions for heat-induced tropical circulation. *Quart. J. Roy. Meteor. Soc.*, **106**, 447–462, https://doi.org/10.1002/qj.49710644905.

Gong, D., and S. Wang, 1999: Definition of Antarctic Oscillation index. *Geophys. Res. Lett.*, **26**, 459–462, https://doi.org/10.1029/1999GL900003.

Gudmundsson, G. H., 2013: Ice-shelf buttressing and the stability of marine ice sheets. *Cryosphere*, **7**, 647–655, https://doi.org/10.5194/tc-7-647-2013.

Hersbach, H., and Coauthors, 2019: Global reanalysis: Goodbye ERA-Interim, hello ERA5. *ECMWF Newsletter*, No. 159, ECMWF, Reading, United Kingdom, 17–24, https://www.ecmwf.int/sites/default/files/elibrary/2019/19027-global-reanalysis-goodbye-era-interim-hello-era5.pdf.

Hoskins, B. J., and D. J. Karoly, 1981: The steady linear response of a spherical atmosphere to thermal and orographic forcing. *J. Atmos. Sci.*, **38**, 1179–1196, https://doi.org/10.1175/1520-0469(1981)038<1179:TSLROA>2.0.CO;2.

——, and T. Ambrizzi, 1993: Rossby wave propagation on a realistic longitudinally varying flow. *J. Atmos. Sci.*, **50**, 1661–1671, https://doi.org/10.1175/1520-0469(1993)050<1661:RWPOAR>2.0.CO;2.

Hu, X., S. A. Sejas, M. Cai, Z. Li, and S. Yang, 2019: Atmospheric dynamics footprint on the January 2016 ice sheet melting in West Antarctica. *Geophys. Res. Lett.*, **46**, 2829–2835, https://doi.org/10.1029/2018GL081374.

Jin, D., and B. P. Kirtman, 2009: Why the Southern Hemisphere ENSO responses lead ENSO. *J. Geophys. Res.*, **114**, D23101, https://doi.org/10.1029/2009JD012657.

Jin, F., and B. J. Hoskins, 1995: The direct response to tropical heating in a baroclinic atmosphere. *J. Atmos. Sci.*, **52**, 307–319, https://doi.org/10.1175/1520-0469(1995)052<0307:TDRTTH>2.0.CO;2.

Klein, S. A., B. J. Soden, and N.-C. Lau, 1999: Remote sea surface temperature variations during ENSO: Evidence for a tropical atmospheric bridge. *J. Climate*, **12**, 917–932, https://doi.org/10.1175/1520-0442(1999)012<0917:RSSTVD>2.0.CO;2.

Li, X., D. M. Holland, E. P. Gerber, and C. Yoo, 2014: Impacts of the north and tropical Atlantic Ocean on the Antarctic Peninsula and sea ice. *Nature*, **505**, 538–542, https://doi.org/10.1038/nature12945.

——, E. P. Gerber, D. M. Holland, and C. Yoo, 2015a: A Rossby wave bridge from the tropical Atlantic to West Antarctica. *J. Climate*, **28**, 2256–2273, https://doi.org/10.1175/JCLI-D-14-00450.1.

——, D. M. Holland, E. P. Gerber, and C. Yoo, 2015b: Rossby waves mediate impacts of tropical oceans on West Antarctic atmospheric circulation in austral winter. *J. Climate*, **28**, 8151–8164, https://doi.org/10.1175/JCLI-D-15-0113.1.

——, and Coauthors, 2021: Tropical teleconnection impacts on Antarctic climate changes. *Nat. Rev. Earth Environ.*, **2**, 680–698, https://doi.org/10.1038/s43017-021-00204-5.

Li, W., Y. Wu, and X. Hu, 2023: The processes-based attributes of four major surface melting events over the Antarctic Ross Ice Shelf. *Adv. Atmos. Sci.*, **40**, 1662–1670, https://doi.org/10.1007/s00376-023-2287-3.

Liebmann, B., and C. A. Smith, 1996: Description of a complete (interpolated) outgoing longwave radiation dataset. *Bull. Amer. Meteor. Soc.*, **77**, 1275–1277.

Liu, H., L. Wang, and K. C. Jezek, 2006: Spatiotemporal variations of snowmelt in Antarctica derived from satellite scanning multichannel microwave radiometer and special sensor microwave imager data (1978–2004). *J. Geophys. Res.*, **111**, F01003, https://doi.org/10.1029/2005JF000318.

Marshall, G. J., A. Orr, N. P. M. van Lipzig, and J. C. King, 2006: The impact of a changing Southern Hemisphere annular mode on Antarctic Peninsula summer temperatures. *J. Climate*, **19**, 5388–5404, https://doi.org/10.1175/JCLI3844.1.

——, D. W. J. Thompson, and M. R. van den Broeke, 2017: Circulation patterns in Antarctic precipitation. *Geophys. Res. Lett.*, **44**, 11 580–11 589, https://doi.org/10.1002/2017GL075998.

Mo, K. C., and R. W. Higgins, 1998: The Pacific–South American modes and tropical convection during the Southern Hemisphere winter. *Mon. Wea. Rev.*, **126**, 1581–1596, https://doi.org/10.1175/1520-0493(1998)126<1581:TPSAMA>2.0.CO;2.

Neale, R. B., J. Richter, S. Park, P. H. Lauritzen, S. J. Vavrus, P. J. Rasch, and M. Zhang, 2013: The mean climate of the Community Atmosphere Model (CAM4) in forced SST and fully coupled experiments. *J. Climate*, **26**, 5150–5168, https://doi.org/10.1175/JCLI-D-12-00236.1.

Nicolas, J. P., and Coauthors, 2017: January 2016 extensive summer melt in West Antarctica favoured by strong El Niño. *Nat. Commun.*, **8**, 15799, https://doi.org/10.1038/ncomms15799.

Orr, A., and Coauthors, 2023: Characteristics of surface "melt potential" over Antarctic ice shelves based on regional atmospheric model simulations of summer air temperature extremes from 1979/80 to 2018/19. *J. Climate*, **36**, 3357–3383, https://doi.org/10.1175/JCLI-D-22-0386.1.

Picard, G., and M. Fily, 2006: Surface melting observations in Antarctica by microwave radiometers: Correcting 26-year time series from changes in acquisition hours. *Remote Sens. Environ.*, **104**, 325–336, https://doi.org/10.1016/j.rse.2006.05.010.

Plumb, R. A., 1985: On the three-dimensional propagation of stationary waves. *J. Atmos. Sci.*, **42**, 217–229, https://doi.org/10.1175/1520-0469(1985)042<0217:OTTDPO>2.0.CO;2.

Rayner, N. A., D. E. Parker, E. B. Horton, C. K. Folland, L. V. Alexander, D. P. Rowell, E. C. Kent, and A. Kaplan, 2003: Global analyses of sea surface temperature, sea ice, and night marine air temperature since the late nineteenth century. *J. Geophys. Res.*, **108**, 4407, https://doi.org/10.1029/2002JD002670.

Rogers, J. C., and H. van Loon, 1982: Spatial variability of sea level pressure and 500 mb height anomalies over the Southern Hemisphere. *Mon. Wea. Rev.*, **110**, 1375–1392, https://doi.org/10.1175/1520-0493(1982)110<1375:SVOSLP>2.0.CO;2.

Sardeshmukh, P. D., and B. J. Hoskin, 1988: The generation of global rotation flow by steady idealized tropical divergence. *J. Atmos. Sci.*, **45**, 1228–1251, https://doi.org/10.1175/1520-0469(1988)045%3C1228:TGOGRF%3E2.0.CO;2.

Schoof, C., 2007: Ice sheet grounding line dynamics: Steady states, stability, and hysteresis. *J. Geophys. Res.*, **112**, F03S28, https://doi.org/10.1029/2006JF000664.

Scott, R. C., J. P. Nicolas, D. H. Bromwich, J. R. Norris, and D. Lubin, 2019: Meteorological drivers and large-scale climate forcing of West Antarctic surface melt. *J. Climate*, **32**, 665–684, https://doi.org/10.1175/JCLI-D-18-0233.1.

Seager, R., N. Harnik, Y. Kushnir, W. Robinson, and J. Miller, 2003: Mechanisms of hemispherically symmetric climate variability. *J. Climate*, **16**, 2960–2978, https://doi.org/10.1175/1520-0442(2003)016<2960:MOHSCV>2.0.CO;2.

Simpkins, G. R., Y. Peings, and G. Magnusdottir, 2016: Pacific influences on tropical Atlantic teleconnections to the Southern Hemisphere high latitudes. *J. Climate*, **29**, 6425–6444, https://doi.org/10.1175/JCLI-D-15-0645.1.

Stevens, C., C. Hulbe, M. Brewer, C. Stewart, N. Robinson, C. Ohneiser, and S. Jendersie, 2020: Ocean mixing and heat transport processes observed under the Ross Ice Shelf control its basal melting. *Proc. Natl. Acad. Sci. USA*, **117**, 16 799–16 804, https://doi.org/10.1073/pnas.1910760117.

Sun, Y., and B. Tan, 2022: A new subseasonal atmospheric teleconnection bridging tropical deep convection over the western North Pacific and Antarctic weather. *Atmos. Sci. Lett.*, **23**, e1115, https://doi.org/10.1002/asl.1115.

Tedesco, M., 2009: Assessment and development of snowmelt retrieval algorithms over Antarctica from K-band spaceborne brightness temperature (1979–2008). *Remote Sens. Environ.*, **113**, 979–997, https://doi.org/10.1016/j.rse.2009.01.009.

The IMBIE Team, 2018: Mass balance of the Antarctic ice sheet from 1992 to 2017. *Nature*, **558**, 219–222, https://doi.org/10.1038/s41586-018-0179-y.

Torinesi, O., M. Fily, and C. Genthon, 2003: Variability and trends of the summer melt period of Antarctic ice margins since 1980 from microwave sensors. *J. Climate*, **16**, 1047–1060, https://doi.org/10.1175/1520-0442(2003)016<1047:VATOTS>2.0.CO;2.

Trusel, L. D., K. E. Frey, and S. B. Das, 2012: Antarctic surface melting dynamics: Enhanced perspectives from radar scatterometer data. *J. Geophys. Res.*, **117**, F02023, https://doi.org/10.1029/2011JF002126.

Wille, J. D., V. Favier, A. Dufour, I. V. Gorodetskaya, J. Turner, C. Agosta, and F. Codron, 2019: West Antarctic surface melt triggered by atmospheric rivers. *Nat. Geosci.*, **12**, 911–916, https://doi.org/10.1038/s41561-019-0460-1.

——, and Coauthors, 2021: Antarctic atmospheric river climatology and precipitation impacts. *J. Geophys. Res. Atmos.*, **126**, e2020JD033788, https://doi.org/10.1029/2020JD033788.

Yu, J.-Y., H. Paek, E. S. Saltzman, and T. Lee, 2015: The early 1990s change in ENSO-PSA-SAM relationships and its impact on Southern Hemisphere climate. *J. Climate*, **28**, 9393–9408, https://doi.org/10.1175/JCLI-D-15-0335.1.

Zhang, G. J., and N. A. McFarlane, 1995: Sensitivity of climate simulations to the parameterization of cumulus convection in the Canadian Climate Centre general circulation model. *Atmos.–Ocean*, **33**, 407–446, https://doi.org/10.1080/07055900.1995.9649539.

Zou, X., D. H. Bromwich, J. P. Nicolas, A. Montenegro, and S.-H. Wang, 2019: West Antarctic surface melt event of January 2016 facilitated by Föhn warming. *Quart. J. Roy. Meteor. Soc.*, **145**, 687–704, https://doi.org/10.1002/qj.3460.

——, ——, A. Montenegro, S.-H. Wang, and L. Bai, 2021a: Major surface melting over the Ross Ice Shelf Part I: Foehn effect. *Quart. J. Roy. Meteor. Soc.*, **147**, 2874–2894, https://doi.org/10.1002/qj.4104.

——, ——, ——, ——, and ——, 2021b: Major surface melting over the Ross Ice Shelf Part II: Surface energy balance. *Quart. J. Roy. Meteor. Soc.*, **147**, 2895–2916, https://doi.org/10.1002/qj.4105.